An efficient compact blazed grating antenna for optical phased arrays

IOP Publishing J. Phys. Photonics 6 (2024) 045010 https://doi.org/10.1088/2515-7647/ad6ed4

Journal of Physics: Photonics

OPEN ACCESS

RECEIVED
11 December 2023

REVISED
6 August 2024

ACCEPTED FOR PUBLICATION
13 August 2024

PUBLISHED
2 September 2024

PAPER

An efficient compact blazed grating antenna for optical phased arrays

Henna Farheen[1], **Suraj Joshi**[1], **J Christoph Scheytt**[2], **Viktor Myroshnychenko**[1] and **Jens Förstner**[1,*]

[1] Theoretical Electrical Engineering, Paderborn University, Warburger Str. 100, 33098 Paderborn, Germany
[2] System and Circuit Technology, Paderborn University, Fürstenallee 11, 33102 Paderborn, Germany
* Author to whom any correspondence should be addressed.

E-mail: jens.foerstner@uni-paderborn.de

Keywords: optical phased arrays, antennas, directivity, field of view, upward radiation efficiency

Abstract

Phased arrays are vital in communication systems and have received significant interest in the field of optoelectronics and photonics, enabling a wide range of applications such as LiDAR, holography, and wireless communication. In this work, we present a blazed grating antenna that is optimized to have upward radiation efficiency as high as 80% with a compact footprint of 3.5 μm $\times$ 2 μm at an operational wavelength of 1.55 μm. Our numerical investigations demonstrate that this antenna in a 64 $\times$ 64 phased array configuration is capable of producing desired far-field radiation patterns. Additionally, our antenna possesses a low side lobe level of -9.7 dB and a negligible reflection efficiency of under 1%, making it an attractive candidate for integrated optical phased arrays.

1. Introduction

Integrated optical antennas in the transmitting mode are devices that couple localized power into free propagating radiation in their surrounding medium, where the freely radiating electromagnetic waves interfere in the far-field [1–5]. These antennas pave the way to numerous integrated photonic systems like optical phased arrays (OPAs) [6–9], wireless communication [10–12], optical switches [13], coherent imagers [14], LiDAR [15–17], etc. Such systems are commonly realized using silicon photonic integration, which is highly compatible with the complementary metal-oxide-semiconductor (CMOS) process, thus furnishing high-yield, low-cost commercial systems [18–20]. In particular, for OPAs, this has proven to be extremely beneficial in incorporating a large number of antennas that aid in generating desired far-field radiation patterns [21]. Conventionally, the performance of an OPA is strongly influenced by the number of elements and the spacing between them, which control the angular resolution, beamwidth, and periodicity of the grating lobes. Many of these arrays are implemented as 1-D OPAs, as they can tightly assemble long and narrow radiators [22–24]. However, such a configuration can perform beam steering solely in one direction unless used with a highly precise tunable laser [25–27]. On the other hand, 2D OPAs are capable of beam steering in two directions via phase tuning at the operational wavelength [28]. Nonetheless, they come at the cost of a limited field of view (FOV), i.e. the grating-lobe-free region for beam steering [21], due to footprints of the radiating elements being larger than half the optical wavelength. However, it has been demonstrated that the issue of limited beam steering can be partially mitigated using a sparse array configuration. Such arrays integrate a large number of elements in an $N \times N$ grid in a non-uniform fashion with minimal inter-element spacing, taking into account the implications of waveguide routing [25]. Although these arrays have a comparatively lower gain for a given chip size, they can significantly reduce the array's beamwidth and increase the number of resolvable spots [29]. An alternative approach to address the problem of beam steering is to employ circularly symmetric array configurations. These structures exploit the properties of a zero-order Bessel-like intensity distribution in the far-field, implicating a visible region with no grating lobes [30]. Yet another approach for achieving grating-lobe-free beam steering is to utilize the principle of co-prime sampling in optical transceiver arrays [31].

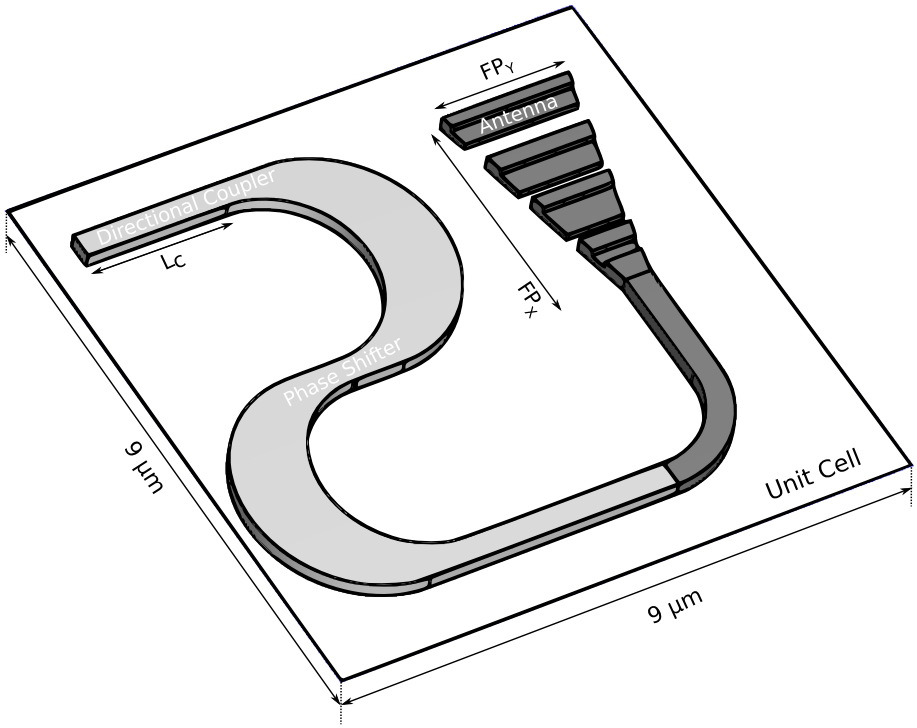

Figure 1. Schematic representation of the 9 μm × 9 μm unit cell, comprised of three main components, namely a direction coupler, a phase shifter, and the dielectric antenna. The parameters FP_x and FP_y indicate the antenna's footprint along the x- and y-axis, respectively.

Together, challenges like large FOV, high radiation efficiency, and reduced form factor with compact unit cells continue to create a surge for devising new radiator designs that can fulfill these requirements [32]. Recently, it has been shown that dielectric horn antennas possess highly directive fields [33–35], while blazed gratings are capable of near-vertical high radiation efficiency [36–40]. In this work, we report on a compact blazed grating horn antenna which is optimized for a wavelength of 1.55 μm to produce high upward radiation efficiency with a broadside emission angle constraint. This is done by performing full-wave numerical simulations utilizing the finite element method (FEM) together with a hybrid optimization routine. Our antenna radiates almost 80% of the input optical power in the upward direction with the aid of blazed gratings. We envision that such antennas can be easily fabricated and efficiently employed in many current and emerging technologies.

2. Numerical setup

In this work, we optimize the radiation characteristics of an antenna to be employed in a 2D OPA described in [21], where each unit cell has a size of 9 μm × 9 μm, as illustrated in figure 1. Every unit cell consists of a directional coupler (DC), a phase shifter (PS), and an antenna of footprint FP_x × FP_y in the xy-plane, with the x-axis representing the direction of wave propagation. The proposed antenna consists of a waveguide-fed silicon horn antenna ($n_{Si} = 3.4$) comprising four gratings in a silicon dioxide ($n_{SiO_2} = 1.44$) environment. The first grating is a partially etched trapezoidal grating with a U-shape, while the other three gratings are L-shaped trapezoidal gratings. Figure 2(a) illustrates the schematic of the antenna with an orientation along the xy-plane. The antenna is excited by the fundamental TE mode at an operating wavelength of 1.55 μm. The full-wave numerical simulations were performed using the FEM solver of CST Microwave Studio [41]. The optimization goal function, the upward efficiency (η_{up}), can be defined as

$$\eta_{up} = \frac{\int_0^{2\pi}\int_0^{\pi/2} P_{rad}(\theta,\varphi)\,d\theta d\varphi}{P_{in}}, \quad (1)$$

where P_{rad} is the power radiating in the defined computation domain, P_{in} is the input optical power, θ is the polar angle, and φ is the azimuthal angle. Therefore, the total upward radiated power is taken into consideration for the optimization in contrast to the power in the array's FOV as presented in [32].

The goal function is maximized by utilizing the dimensions of the horn structure, and are thus decision variables for the problem. The optimal parameters are estimated using a hybrid optimization routine, which

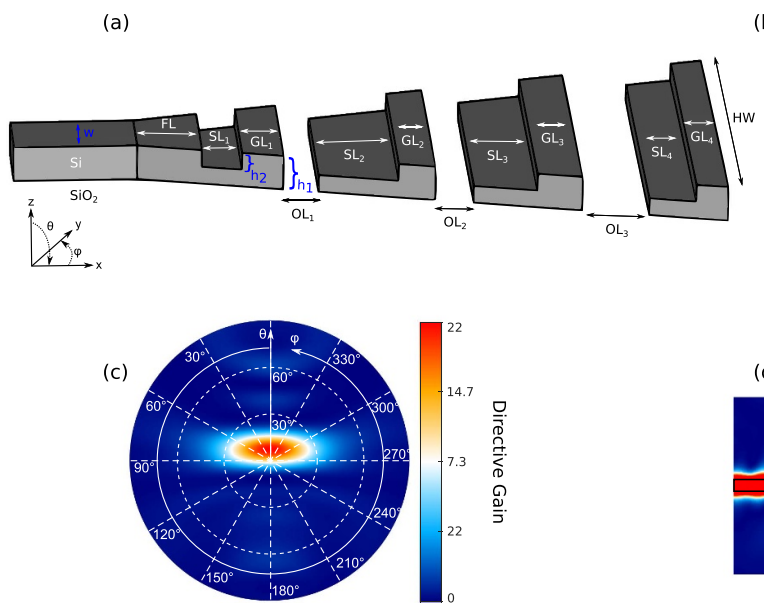

Parameters	Dimensions
Horn Width (HW)	2000 nm
Flare Length (FL)	390 nm
Grating Length 1 (GL_1)	250 nm
Grating Length 2 (GL_2)	220 nm
Grating Length 3 (GL_3)	270 nm
Grating Length 4 (GL_4)	190 nm
Segment Length 1 (SL_1)	240 nm
Segment Length 2 (SL_2)	480 nm
Segment Length 3 (SL_3)	380 nm
Segment Length 4 (SL_4)	280 nm
Offset Length 1 (OL_1)	210 nm
Offset Length 2 (OL_2)	230 nm
Offset Length 3 (OL_3)	400 nm
Waveguide Width (w)	400 nm
Height 1 (h_1)	220 nm
Height 2 (h_2)	110 nm

Figure 2. (a) Schematic representation of the optimized horn antenna, highlighting the parameters used in the optimization. (b) Values of the design parameters obtained for the optimized antenna. (c) Calculated angular linear directive gain distribution of the optimized antenna exhibiting a directivity of $D = 22$ at $\theta = 8°$. (d) Calculated near-field distribution of the power flow for the optimized antenna in the xz-plane at $y = 0$.

includes particle swarm optimization (PSO) followed by the trust region method (TRM). The PSO functions as a global search mechanism to locate a feasible set of optimal dimensions [42]. These variables are constrained by the fabrication limitations of standard silicon-on-insulator (SOI) platforms, as described in [43]. The optimization begins with random initial sets to define the position of the particles in the swarm. In every iteration, the objective function is evaluated for all particles, where each particle stores the best position it has visited so far, while also being aware of the current global best position. The best position refers to a set of dimensions where the objective function is maximized. The update in each particle's position is carried out using a velocity vector that propels the particles to new positions in the search space. This vector depends on the particle's current position, its best position so far, and the current global best position. At the end of the search process, the final global best position corresponds to the global maximum discovered by the optimizer. At this point, the TRM implements a local search within this located subspace. This search is carried out via the contraction or expansion of the trust region using a set of deterministic step sizes that are calculated in every iteration. Therefore, the proposed optimization approach performs a thorough exploration of the search space to obtain a globally optimized solution.

3. Results and discussion

As stated before, the optimization process considers the dimensions of the horn antenna. Along the x-axis, the different lengths are classified as grating lengths (GL_x), offset lengths (OL_x), segment lengths (SL_x), and flare length (FL), which is the initial taper length. These parameters along with the horn width (HW), result in thirteen optimization parameters whose optimal values are shown in figure 2(b). The values in blue highlight the fixed dimensions of the structure like the width of the feeding waveguide (w), height of the antenna ($h_1 = 220$ nm), and height of the partial etch ($h_2 = 110$ nm) in all the gratings. The PSO optimizer employs a swarm of 40 particles and converges to the global optimum in ∼1200 computations, i.e. ∼30 iterations. The PSO optimum is further reinforced by a subsequent local search performed with the TRM, which converges to the same optimum after approximately 900 computations. These calculations were performed on an "Intel Xeon Gold 6148 CPU @ 2.40GHz" node of 40 cores, which required less than one minute for each computation. The resulting optimized structure has a compact footprint of 3.5 μm × 2 μm with a linear directivity of 22, as shown in the calculated linear directive gain distribution in figure 2(c), centered at $\theta = 8°$. The antenna demonstrates a low side lobe level of −9.7 dB and an appreciable half power beamwidth (HPBW) of 18° × 56°. Furthermore, figure 2(d) shows the near-field power distribution in the xz-plane at $y = 0$. It becomes evident that along the length of the radiator, the input power constructively interferes in the upper hemisphere due to the multi-layer up-down asymmetries, while destructive interference dominates in the lower hemisphere.

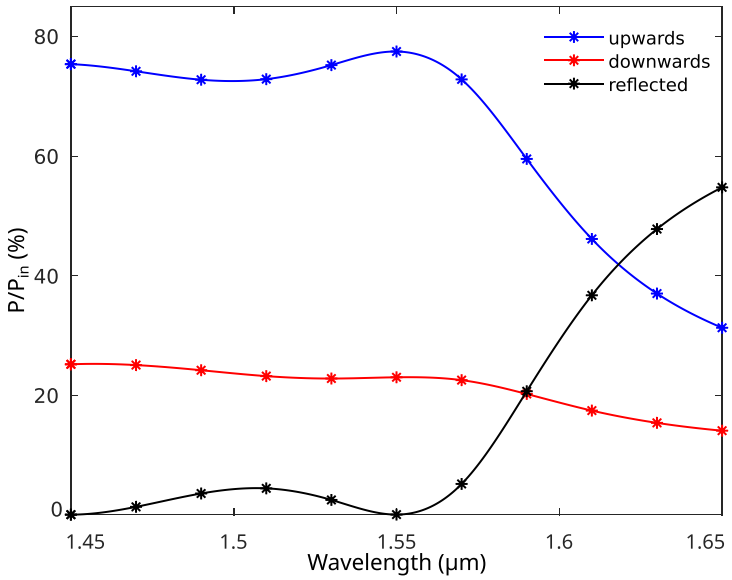

Figure 3. Calculated optical radiation and reflection efficiencies of the optimized antenna as a function of the wavelength.

To get an insight into the broadband behavior of the antenna, the upward and downward radiation efficiencies, and the reflection efficiency, as functions of the wavelength, are shown in figure 3. The blue and red curves highlight the upward and downward radiation efficiencies, respectively, while the black curve illustrates the percentage of power reflected back to the waveguide. As the antenna is optimized for 1.55 μm, it has its best performance at this wavelength and is sensitive to the longer wavelengths thereon. The upward radiation is higher for shorter wavelengths and reduces drastically for longer wavelengths, which results in an increased reflection to the waveguide. However, the antenna maintains a consistently low downward radiation efficiency throughout the operating range. This implies that the antenna design works well in breaking the up-down symmetry, thus preventing more downward radiation. To lower the reflection efficiency over a wide range of wavelengths, a sub-wavelength grating (SWG) design approach can also be incorporated, as demonstrated in [38]. At 1.55 μm, the antenna exhibits a high upward radiation efficiency of approximately 80%, partly influenced by the partial etch in the U-shaped grating, which helps create a phase difference between the upward and downward propagating radiation [21]. The aperiodic L-shaped trapezoidal diffraction gratings further strengthen the up-down asymmetry along the entire length of the structure. This reinforces the constructive interference in the upward direction, and destructive interference in the downward direction, and consequently, reduces the in-plane propagation (see figure 2(d)). Furthermore, the antenna has almost no power that is reflected back into the feeding waveguide, thus making it highly efficient.

In the next step, we employ our optimized antenna in a 2D phased array configuration for which we consider the 9 μm $\times$ 9 μm unit cell (see figure 1). The optimized antenna already has a size that can easily fit into this unit cell, and also the benefit of much higher upward radiation efficiency compared to the 51% from the radiator described in [21]. The field for such an array can be defined as

$$\mathbf{E}_{\text{array}}(\theta,\varphi) = \mathbf{E}_{\text{antenna}}(\theta,\varphi)\,\text{AF}(\theta,\varphi), \tag{2}$$

where $\mathbf{E}_{\text{array}}(\theta,\varphi)$ is the far-field of the OPA, $\mathbf{E}_{\text{antenna}}(\theta,\varphi)$ is the far-field of a single antenna, and $\text{AF}(\theta,\varphi)$ is the scalar function representing the array factor. We note that this equation ignores the coupling effects between the adjacent unit cells unlike the demonstration in [44].

Such arrays can potentially be used in imaging applications, where complex far-field radiation patterns need to be constructed. Figure 4 illustrates the results of pattern synthesis accomplished by utilizing the optimized antenna in a uniformly excited 64 $\times$ 64 array. For pattern synthesis, the Gerchberg–Saxton algorithm (GSA) [45, 46] utilizes the amplitude of a reference array factor (provided as an image), and unity input magnitudes to determine the excitation phases required to accurately reconstruct any desired far-field pattern. The algorithm begins with an inverse Fourier transform of the reference array factor to obtain the initial near-field magnitude and phase data. In every iteration, the excitation amplitudes obtained by the inverse Fourier transform are replaced with unity, while retaining the phase data as is. A Fourier transform of this modified data returns an approximate array factor. The amplitudes of the approximate and reference

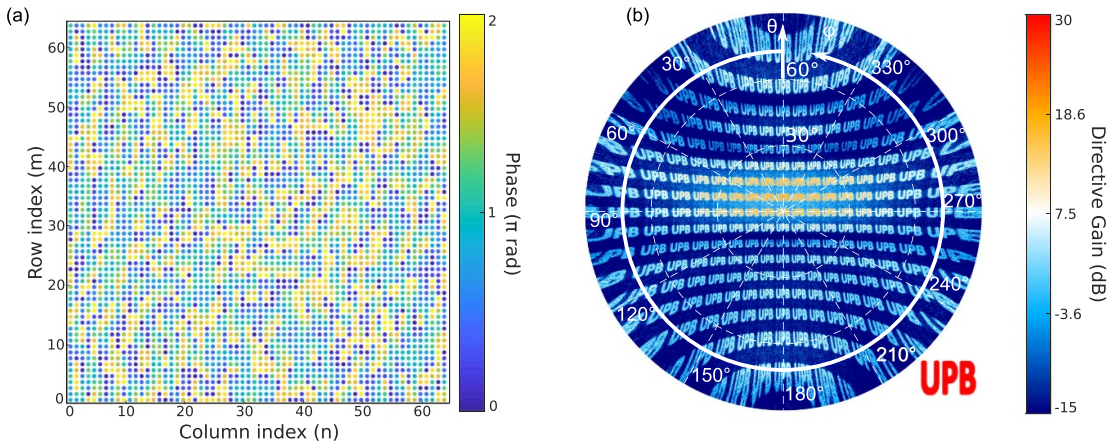

Figure 4. Calculated (a) phase and (b) far-field distribution for generating the 'UPB' initials with a 64 × 64 phased array configuration utilizing the optimized antenna with an inter-element spacing of 9 μm. The original image used in the process is shown next to the far-field pattern.

array factors are utilized to calculate the error for a given iteration. Once the error is minimized, the algorithm is terminated and the iterative process comes to a halt. The generated near-field phase distribution is used to accurately produce the reference array factor in the far-field. In this work, the initials of the University of Paderborn 'UPB' were used as the reference array factor. The phase distribution generated by the GSA is shown in figure 4(a), and the associated far-field for the uniformly excited OPA is illustrated in figure 4(b). The image used for the pattern generation is shown next to the generated far-field. Besides, figure 4(b) presents 16 grating lobes in the far-field radiation pattern for each direction due to the large inter-element spacing of 9 μm. This number of interference orders m can be estimated by

$$| m\lambda_n/d | < 2, \tag{3}$$

where m is the largest value that satisfies equation (3), λ_n is the medium wavelength and d is the size of the unit cell. As an idealized half-wavelength spacing cannot be achieved in the given 2D OPA configuration, these grating lobes are inevitable. The far-field pattern also reveals a bright region along the horizontal direction, which can be attributed to the large HPBW of 56° from each antenna. This large beamwidth is particularly desirable for array configurations that demonstrate beam steering in a range only limited by the FOV of the radiating element [30]. Finally, we would like to note here that our calculations based on equation (2) ignore the mutual coupling effects between the adjacent unit cells. We assumed that the coupling effects are negligible for such a large unit cell of 9 μm × 9 μm size that is $\sim (5.8\lambda)^2$. To verify this assumption, we evaluated the near-field power radiated upwards for several infinite 2D arrays consisting of a unit cell of a different size ranging from 4.5 μm × 4.5 μm to 9 μm × 9 μm. This is done by applying periodic boundary conditions on the unit cells in the x- and y-directions. Our results (not shown here) reveal that the upward radiated power remains nearly the same for all configurations for a wavelength range of 1.45–1.65 μm. Therefore, the product of the scalar array factor and the radiating element's far-field pattern is a reasonable method for estimating the far-field pattern of our OPA.

The large unit cell size of 9 μm constrains the FOV of the array, which in turn limits the angular range for beam steering to approximately 6.8° × 6.8°. We illustrate the possibility of steering the beam for which we use an 8 × 8 OPA that provides better visualization of the steering effect, as seen in figure 5. The far-field patterns are limited to an angular range of $\theta = 20°$ to highlight the shifting positions of the main beam. Figure 5(a) demonstrates the phase distribution and far-field pattern for the array when no phase input is applied to the OPA. This serves as the reference for observing the beam steering effect. Alternating the phase with zero and π along the rows or columns, as shown in figures 5(b) and (c), steers the beam along the vertical or horizontal directions, respectively. Similarly, alternating the phase inputs along the rows and columns with zero and π results in the beam being steered diagonally, as shown in figure 5(d). Furthermore, one can also provide phase distributions that split the main beam or move it in an arbitrary direction in the FOV of the array.

Finally, table 1 compares our results with the simulation results of other antennas used specifically in the context of 2D OPA configurations. Our proposed antenna has the smallest footprint and highest efficiency, with a relatively low angle of emission. We accomplish an overall size reduction of 28% and 49% in comparison to the footprints reported in [21] and [38], respectively. Also, an efficiency improvement of 9%

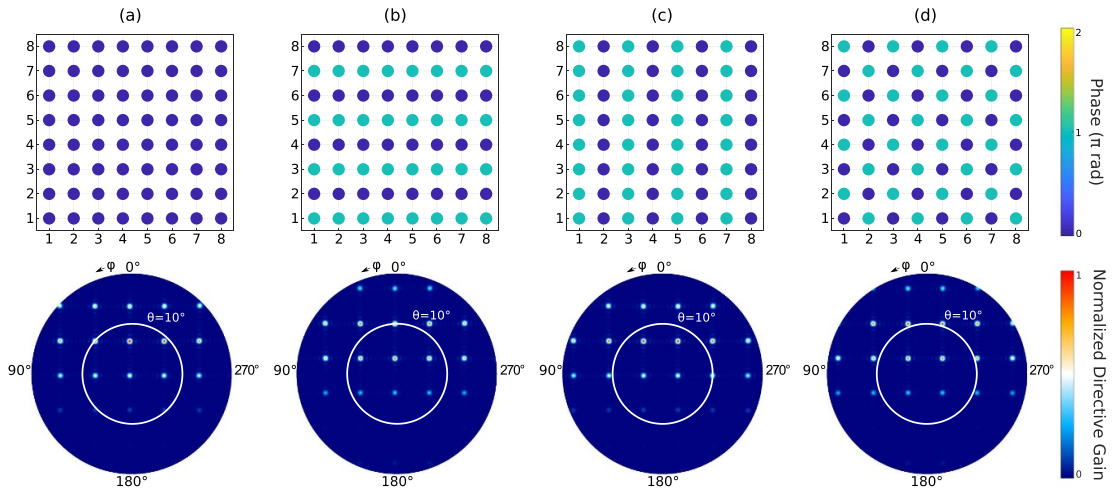

Figure 5. Demonstration of beam steering with an 8 × 8 array configuration of the optimized antenna. (a) Phase distribution and simulated linear far-field radiation pattern of a uniform phased array. (b)–(d) Phase distribution and the simulated linear far-field radiation pattern for the main-lobe to be shifted (b) vertically, (c) horizontally, and (d) diagonally.

Table 1. Comparison of characteristics of different antennas.

Design	Footprint	η_{up}	θ	$\sim S_{11}$	Numerical method	Fabricated
sun *et al* [21]	3.5 μm × 2.8 μm	51%	15°	−13 dB	FDTD	Yes
Fatemi *et al* [25]	5 μm × 2 μm	51%	7.4°	unknown	unknown	Yes
Benedikovič *et al* [38]	5.5 μm × 2.5 μm	71%	6°	−20 dB	FDTD	No
Fatemi *et al* [6]	5.1 μm × 2 μm	35%	9°	unknown	unknown	No
This work	3.5 μm × 2 μm	80%	8°	−26 dB	FEM	No

and 45% is achieved when compared to the radiators from [38] and [6], respectively. An additional useful metric for comparison is the power reflected back to the waveguide segment, which can be measured using the S_{11} parameter. At 1.55 μm, [38] and [21] report S_{11} values of approximately −20 dB (1%) and −13 dB (5%). Our proposed structure possesses an S_{11} of −26 dB (0.25%), which is a quarter of the acceptable reflected power for many phased array systems [6]. Therefore, we anticipate that any OPA system can operate undisturbed with such a radiating element.

4. Conclusion

We present the design and optimization of a compact horn-shaped blazed grating antenna that utilizes a heterogeneous grating configuration consisting of a U-shaped grating and L-shaped gratings. The use of a FEM solver in conjunction with a hybrid optimization routine reveals a structure with nearly 80% upward radiation efficiency, an appreciable HPBW of 18° × 56°, and negligible reflected power. The proposed antenna is suitable for standard 2D OPAs utilized for pattern synthesis and beamforming, including architectures that introduce the prospect of increasing the grating-lobe-free beam steering range using a large HPBW. Overall, the given antenna design meets fabrication-imposed constraints of standard 220 nm SOI-CMOS platforms and opens up the possibility of fabricating highly efficient OPA systems with desirable radiation characteristics. To our knowledge, the current work presents a radiating element with the highest upward radiation efficiency with the smallest footprint applicable for direct use in 2D OPAs.

Data availability statement

The data that support the findings of this study are openly available at the following URL/DOI: https://doi.org/10.5281/zenodo.7966024.

Acknowledgments

The work was funded by the Ministry of Culture and Science of the state of North Rhine-Westphalia via the PhoQC project. Additionally, the authors gratefully acknowledge financial support from the Deutsche Forschungsgemeinschaft (DFG) via TRR142 projects C05 and B06, and the computing time support provided by the Paderborn Center for Parallel Computing (PC^2).

ORCID iDs

Henna Farheen https://orcid.org/0000-0001-7730-3489
Viktor Myroshnychenko https://orcid.org/0000-0001-6431-746X
Jens Förstner https://orcid.org/0000-0001-7059-9862

References

[1] Balanis C A 2015 *Antenna Theory: Analysis and Design* (wiley)
[2] Bharadwaj P, Deutsch B and Novotny L 2009 Optical antennas *Adv. Opt. Photon.* **1** 438–83
[3] Novotny L and Van Hulst N 2011 Antennas for light *Nat. Photon.* **5** 83–90
[4] Leuteritz T, Farheen H, Qiao S, Spreyer F, Schlickriede C, Zentgraf T, Myroshnychenko V, Förstner J and Linden S 2021 Dielectric travelling wave antennas for directional light emission *Opt. Express* **29** 14694–704
[5] Fenn A J, Temme D H, Delaney W P and Courtney W E 2000 The development of phased-array radar technology *Linc. Lab. J.* **12** 321–40 (available at: www.ll.mit.edu/sites/default/files/publication/doc/development-phased-array-radar-technology-fenn-ja-7838.pdf)
[6] Fatemi R, Khial P P, Khachaturian A and Hajimiri A 2020 Breaking FOV-aperture trade-off with multi-mode nano-photonic antennas *IEEE J. Sel. Top. Quantum Electron.* **27** 1–14
[7] Hirano Y, Motoyama Y, Tanaka K, Machida K, Yamada T, Otomo A and Kikuchi H 2018 Demonstration of an optical phased array using electro-optic polymer phase shifters *Jpn. J. Appl. Phys.* **57** 03EH09
[8] Van Acoleyen K, Rogier H and Baets R 2010 Two-dimensional optical phased array antenna on silicon-on-insulator *Opt. Express* **18** 13655–60
[9] Van Acoleyen K, Bogaerts W, Jágerská J, Le Thomas N, Houdré R and Baets R 2009 Off-chip beam steering with a one-dimensional optical phased array on silicon-on-insulator *Opt. Lett.* **34** 1477–9
[10] Poulton C V, Byrd M J, Russo P, Timurdogan E, Khandaker M, Vermeulen D and Watts M R 2019 Long-range LiDAR and free-space data communication with high-performance optical phased arrays *IEEE J. Sel. Top. Quantum Electron.* **25** 1–8
[11] Neubert W M, Kudielka K H, Leeb W R and Scholtz A L 1994 Experimental demonstration of an optical phased array antenna for laser space communications *Appl. Opt.* **33** 3820–30
[12] Rabinovich W S, Goetz P G, Pruessner M, Mahon R, Ferraro M S, Park D, Fleet E and DePrenger M J 2015 Free space optical communication link using a silicon photonic optical phased array *Free-Space Laser Communication and Atmospheric Propagation Xxvii* 9354 (International Society for Optics and Photonics) 93540B
[13] Blanche P-A, LaComb L, Wang Y and Wu M C 2017 Diffraction-based optical switching with MEMS *Appl. Sci.* **7** 411
[14] Aflatouni F, Abiri B, Rekhi A and Hajimiri A 2015 Nanophotonic coherent imager *Opt. Express* **23** 5117–25
[15] Poulton C V, Yaacobi A, Cole D B, Byrd M J, Raval M, Vermeulen D and Watts M R 2017 Coherent solid-state lidar with silicon photonic optical phased arrays *Opt. Lett.* **42** 4091–4
[16] Bhargava P *et al* 2019 Fully integrated coherent LiDAR in 3D-integrated silicon photonics/65nm CMOS *Symp. on VLSI Circuits* (IEEE) pp C262–3
[17] Levinson J *et al* 2011 Towards fully autonomous driving: Systems and algorithms *2011 IEEE Intelligent Vehicles Symp. (IV)* (IEEE) pp 163–8
[18] Chung S, Abediasl H and Hashemi H 2017 A monolithically integrated large-scale optical phased array in silicon-on-insulator CMOS *IEEE J. Solid-State Circuits* **53** 275–96
[19] Ashtiani F and Aflatouni F 2019 N × N optical phased array with 2N phase shifters *Opt. Express* **27** 27183–90
[20] Abediasl H and Hashemi H 2015 Monolithic optical phased-array transceiver in a standard SOI CMOS process *Opt. Express* **23** 6509–19
[21] Sun J, Timurdogan E, Yaacobi A, Su Z, Hosseini E S, Cole D B and Watts M R 2013 Large-scale silicon photonic circuits for optical phased arrays *IEEE J. Sel. Top. Quantum Electron.* **20** 264–78
[22] Abiri B, Fatemi R and Hajimiri A 2018 A 1-D heterodyne lens-free optical phased array camera with reference phase shifting *IEEE Photon. J.* **10** 1–12
[23] Kossey M R, Rizk C and Foster A C 2018 End-fire silicon optical phased array with half-wavelength spacing *APL Photonics* **3** 011301
[24] Poulton C V, Byrd M J, Raval M, Su Z, Li N, Timurdogan E, Coolbaugh D, Vermeulen D and Watts M R 2017 Large-scale silicon nitride nanophotonic phased arrays at infrared and visible wavelengths *Opt. Lett.* **42** 21–24
[25] Fatemi R, Khachaturian A and Hajimiri A 2019 A nonuniform sparse 2-D large-FOV optical phased array with a low-power PWM drive *IEEE J. Solid-State Circuits* **54** 1200–15
[26] Miller S A *et al* 2018 512-element actively steered silicon phased array for low-power LIDAR *Cleo: Science and Innovations* (Optica Publishing Group) p JTh5C–2
[27] Doylend J K, Heck M, Bovington J T, Peters J D, Coldren L and Bowers J 2011 Two-dimensional free-space beam steering with an optical phased array on silicon-on-insulator *Opt. Express* **19** 21595–604
[28] Sun J, Timurdogan E, Yaacobi A, Hosseini E S and Watts M R 2013 Large-scale nanophotonic phased array *Nature* **493** 195–9
[29] Fukui T, Tanomura R, Komatsu K, Yamashita D, Takahashi S, Nakano Y and Tanemura T 2021 Non-redundant optical phased array *Optica* **8** 1350–8
[30] Khachaturian A, Fatemi R, Darbinian A and Hajimiri A 2022 Discretization of annular-ring diffraction pattern for large-scale photonics beamforming *Photon. Res.* **10** 1177–86

[31] Khachaturian A, Fatemi R and Hajimiri A 2022 Achieving full grating-lobe-free field of view with low-complexity co-prime photonic beamforming transceivers *Photon. Res.* **10** A66–A73
[32] Farheen H, Strauch A, Scheytt J C, Myroshnychenko V and Förstner J 2024 Optimized, highly efficient silicon antennas for optical phased arrays *Photon. Nanostruct. Fundam. Appl.* **58** 101207
[33] Farheen H, Leuteritz T, Linden S, Myroshnychenko V and Förstner J 2022 Optimization of optical waveguide antennas for directive emission of light *JOSA* B **39** 83–91
[34] Farheen H, Yan L-Y, Quiring V, Eigner C, Zentgraf T, Linden S, Förstner J and Myroshnychenko V 2022 Broadband optical Ta_2O_5 antennas for directional emission of light *Opt. Express* **30** 19288–99
[35] Farheen H, Joshi S, Scheytt J, Myroshnychenko V and Förstner J 2023 Increasing the upward radiation efficiency of optical phased arrays using asymmetric silicon horn antennas *2023 IEEE Photonics Conf. (IPC)* (IEEE) pp 1–2
[36] Liu Q, Benedikovic D, Smy T, Atieh A, Cheben P and Ye W N 2022 Circular optical phased arrays with radial nano-antennas *Nanomaterials* **12** 1938
[37] Watanabe T, Ayata M, Koch U, Fedoryshyn Y and Leuthold J 2017 Perpendicular grating coupler based on a blazed antiback-reflection structure *J. Lightwave Technol.* **35** 4663–9
[38] Benedikovič D, Liu Q, Sánchez-Postigo A, Atieh A, Smy T, Cheben P and Ye W N 2022 Circular optical phased array with large steering range and high resolution *Sensors* **22** 6135
[39] Melati D, Dezfouli M K, Grinberg Y, Schmid J H, Cheriton R, Janz S, Cheben P and Xu D-X 2020 Design of compact and efficient silicon photonic micro antennas with perfectly vertical emission *IEEE J. Sel. Top. Quantum Electron.* **27** 1–10
[40] Melati D, Grinberg Y, Kamandar Dezfouli M, Janz S, Cheben P, Schmid J H, Sánchez-Postigo A and Xu D-X 2019 Mapping the global design space of nanophotonic components using machine learning pattern recognition *Nat. Commun.* **10** 4775
[41] Systémes D CST Studio Suite (available at: www.cst.com)
[42] Kennedy J and Eberhart R 1995 Particle swarm optimization *Proc. ICNN'95-Int. Conf. on Neural Networks* vol 4 (IEEE) pp 1942–8
[43] Integrated Photonic Systems Roadmap - International (IPSR-I), Silicon Photonics (available at: https://photonicsmanufacturing.org/sites/default/files/documents/2024_ipsr-i_silicon_photonics_updated_v2.pdf)
[44] Kelley D F and Stutzman W L 1993 Array antenna pattern modeling methods that include mutual coupling effects *IEEE Trans. Antennas Propag.* **41** 1625–32
[45] Fienup J R 1978 Reconstruction of an object from the modulus of its fourier transform *Opt. Lett.* **3** 27–29
[46] Gerchberg R W 1972 A practical algorithm for the determination of phase from image and diffraction plane pictures *Optik* **35** 237–46 (available at: www.semanticscholar.org/paper/A-practical-algorithm-for-the-determination-of-from-Gerchberg/5a114d3050a0a33f8cc6d28d55fa048a5a7ab6f2)